High energy resolution five-crystal spectrometer for high quality fluorescence and absorption measurements on an X-ray Absorption Spectroscopy beamline

Isabelle Llorens, Eric Lahera, William Delnet, Olivier Proux, Aurélien Braillard, Jean-Louis Hazemann, Alain Prat, Denis Testemale, Quentin Dermigny, Frédéric Gélébart, et al.

High energy resolution five-crystal spectrometer for high quality fluorescence and absorption measurements on an X-ray Absorption Spectroscopy beamline

Isabelle LLorens
CEA/DSM/INAC/SP2M/NRS F-38054 Grenoble cedex 9, France
Synchrotron SOLEIL – MARS beamline, L'Orme des Merisiers, F-91192 Gif sur Yvette, France

Eric Lahera, William Delnet, and Olivier Proux
Observatoire des Sciences de l'Univers de Grenoble, UMS 832 CNRS Université Joseph Fourier, F-38041 Grenoble cedex 9, France
BM30B/FAME beamline, ESRF, F-38043 Grenoble cedex 9, France

Aurélien Braillard, Jean-Louis Hazemann, Alain Prat, and Denis Testemale
Institut Néel, UPR 2940 CNRS, F-38042 Grenoble cedex 9, France
BM30B/FAME beamline, ESRF, F-38043 Grenoble cedex 9, France

Quentin Dermigny, Frederic Gelebart, Marc Morand, and Abhay Shukla
Institut de Minéralogie et de Physique des Milieux Condensés, UMR 7590, 4 place Jussieu, F-75005 Paris, France

Nathalie Bardou
Laboratoire de Photonique et de Nanostructures, UPR 20 CNRS, Route de Nozay, F-91460 Marcoussis, France

Olivier Ulrich
CEA/DSM/INAC/SP2M/NRS F-38054 Grenoble cedex 9, France
BM32/IF beamline, ESRF, F-38043 Grenoble cedex 9, France

Stéphan Arnaud, Jean-François Berar, Nathalie Boudet and Bernard Caillot
Institut Néel, UPR 2940 CNRS, F-38042 Grenoble cedex 9, France
BM02/D2AM beamline, ESRF, F-38043 Grenoble cedex 9, France

Perrine Chaurand and Jérôme Rose
Centre Européen de Recherche et d'Enseignement des Géosciences de l'Environnement, UMR 7730, F-13545 Aix en Provence, France

Emmanuel Doelsch
CIRAD, UPR Recyclage et risque, Montpellier, France

Philippe Martin
CEA/DEN/DEC/SESC/LLCC F-13108 Saint Paul lez Durance cedex, France

Pier Lorenzo Solari
Synchrotron SOLEIL – MARS beamline, L'Orme des Merisiers, F-91192 Gif sur Yvette, France

Fluorescence detection is classically achieved with a solid state detector (SSD) on X-ray Absorption Spectroscopy (XAS) beamlines. This kind of detection however presents some limitations related to the limited energy resolution and saturation. Crystal analyzer spectrometers (CAS) based on a Johann-type geometry have been developed to overcome these limitations. We have tested and installed such a system on the BM30B/CRG-FAME XAS beamline at the ESRF dedicated to the structural investigation of very dilute systems in environmental, material and biological sciences. The spectrometer has been designed to be a mobile device for easy integration in multi-purpose hard X-ray synchrotron beamlines or even with a laboratory X-ray source. The CAS allows to collect X-ray photons from a large solid angle with five spherically bent crystals. It will cover a large energy range allowing to probe fluorescence lines characteristic of all the elements from Ca (Z = 20) to U (Z = 92). It provides an energy resolution of 1-2 eV. XAS spectroscopy is the main application of this device even if other spectroscopic techniques (RIXS, XES, XRS...) can be also achieved with it. The performances of the CAS are illustrated by two experiments that are difficult or impossible to perform with SSD and the complementarity of the CAS *vs* SSD detectors is discussed.

I. INTRODUCTION

The BM30B/CRG-FAME[1] beamline at the European Synchrotron Radiation Facility (ESRF, Grenoble, France) is dedicated to X-ray absorption spectroscopy (XAS) applied to a wide variety of research fields: condensed matter physics, materials science, biophysics, chemistry and mainly geochemical topics, with special emphasis on highly diluted samples. As such, the optics of the beamline has been designed to optimize both the incident photon flux on the sample and the optical stability to reduce non-statistical noise. A 30-element

CANBERRA solid state detector (SSD) with a typical energy resolution of 150 – 300 eV is used for an optimal acquisition of fluorescence signal. As we show in this article, a way to improve the fluorescence detection significantly in the case of complex or highly diluted samples (see § III) is to use a crystal analyzer spectrometer. With this aim, a focusing Johann type spectrometer has been built and recently commissioned on the beamline so as to improve both the sensitivity in terms of sample concentration and the signal quality.

In general, it is considered that such a spectrometer can be used in the following fields: (i) X-ray absorption fine structure (XAFS) spectroscopy in samples with multi elemental composition matrices, (ii) lifetime-broadening-removed XAFS spectroscopy[2], (iii) site-selective XAFS spectroscopy[3], (iv) X-ray emission spectroscopy (XES)[4], (v) resonant inelastic X-ray scattering (RIXS)[5], (vi) X-ray Raman scattering (XRS)[6,7]. A complete overview of possible applications can be found in reviews by de Groot[8], Kotani and Shin[9], Schülke[10] and Rueff and Shukla[11]. In our case, the spectrometer is dedicated for an improvement of fluorescence detection to improve signal to noise in XAFS measurements and mostly used to distinguish a weak fluorescence emission signal from a multitude of undesirable intense peaks.

A description of the prototype of the present spectrometer which used solitary crystal analyser has already been published[12] as well as results of experiments performed with it[13]. The main limitation of this prototype is the small solid angle of detection corresponding to one crystal (0.03 sr) and thus the limited counting statistics of the measurement. To overcome this, a new spectrometer including five bent crystals has been designed and installed on the beamline. With this design, the integrated solid angle of detection is increased to 0.15 sr. In this paper, we report the complete original design of this spectrometer and results from first experiments.

II. SOURCE

The spectrometer (CAS) is installed on the BM30B/CRG-FAME beamline at the ESRF (schematic description in FIG 1). The source is a 0.8 T bending magnet (critical energy E_c=20 keV giving a maximum of the photons flux around 17 keV). The maximal horizontal divergence integrated by the optical components is 2 mrad. The main optical elements are two parabolic Rh-coated mirrors and a liquid-nitrogen-cooled Si (220) pseudo-channelcut double-crystal monochromator[14]. The spot size (300 x 100 μm^2, HxV FWHM) is kept constant on the sample with (i) the dynamical sagittal focusing of the second crystal of the monochromator[15],

in the horizontal plane, and (ii) the dynamic adjustment of the height of the experimental bench during an energy scan which compensates the vertical deviation of the beam.

The energy resolution is close to the intrinsic value of the monochromator crystal[14], *i.e.* FWHM 0.40 eV at Co and 0.83 eV at Sr K-edges respectively with Si (220) crystal monochromator. The flux measured is about $5x10^{11}$ photons/s/200mA between 7.5 and 13.5 keV (for 1.5 mrad horizontal divergence). Finally, for a given energy, the absolute noise on the intensity of the incident beam ranges between 0.02 and 0.05% for a 1s integrating time.

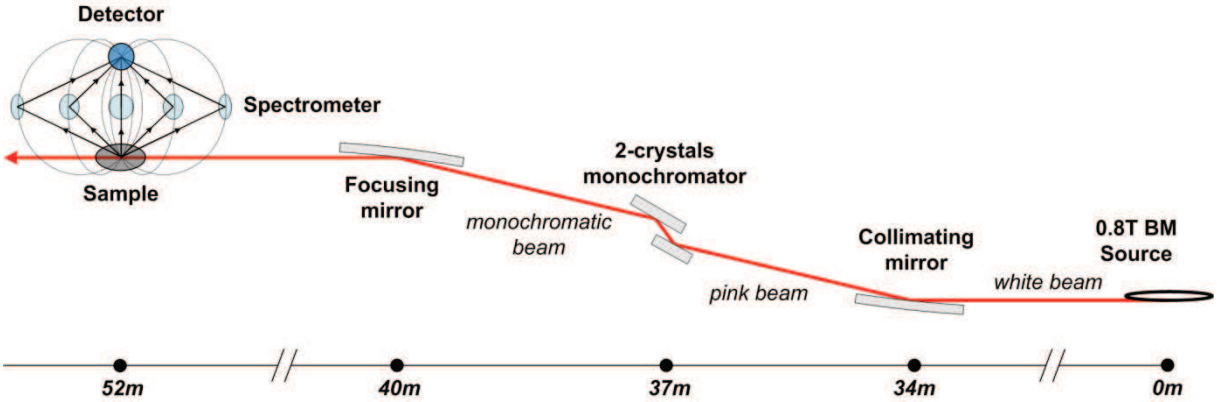

FIGURE 1. Schematic view of CRG BM30B/CRG-FAME beamline at the European Synchrotron Radiation Facility in Grenoble (France).

III. LIMITATIONS OF A SOLID STATE DETECTOR

Energy dispersive solid-state detectors (SSD) are classically used on most of X-ray Absorption Spectroscopy beamlines to record spectra in fluorescence detection mode. Different commercial detectors are available; mainly high-purity germanium (HPGe, cryogenically cooled, optimized for hard X-rays) and silicon drift detectors[16] (SDD, Peltier cooled, optimized for soft to hard X-rays). These solid state detectors are usually easy to use and they allow to probe preferentially diluted elements. The input count rate can be limited by the high photon flux delivered by third generation synchrotron beamlines, but the maximum counting rate can be increased in some cases using an appropriate dead-time correction[16]. Nevertheless, several limitations for optimal XAS acquisition still occur.

A. Saturation

The use of a solid state detector can find limitations when a high counting rate due to the scattered beam and/or a fluorescent signal from the matrix containing the diluted specimen

does not allow detection the signal of interest. For example, in the particular case of Co adsorbed on iron oxide nanoparticles, the absorption spectrum at the Co K-edge ($K\alpha_1$ = 6.930 keV) is difficult to measure with an energy-dispersive detector because the Fe Kβ fluorescence lines (7.058 keV) produce a large signal which saturates the detector.

B. Energy resolution

The second limitation comes from the SSD energy resolution which is fundamentally limited to about 120 eV (FWHM) at 6 keV (Fano statistics)[17] and can be experimentally approached only for low counting rates (*i.e.* large shaping time). A typical energy resolution for a XAS experiment ranges around 150-300 eV, the choice in this range depending on the compromise between an optimal counting rate and a reasonable energy resolution. This energy resolution can be improved by replacing a "conventional" SSD with a superconducting tunnel junction cryogenically cooled detector with an energy resolution ~10-20 eV[18]. However, the complexity of these detectors, mainly due to the required very low temperature of the sensor area (around 100-500 mK), actually limits their use to particle physics and astrophysics.

This limited energy resolution induces a partial overlap of the measured signal with the low-energy tail of the scattered beams (elastic or Thompson scattering, inelastic or Compton scattering...). An illustration (FIG. 2) is given by the study of bromide aqueous solutions at 8ppm (0.1 mM), 40ppm (0.5 mM) and 80ppm (1 mM). The sample-holder is a glassy carbon cell located inside a high pressure vessel equipped with 1.5 mm Be windows for incident, transmitted and fluorescence beams[19]. The Br Kα peaks intensity is of course related to the amount of Br. Consequently, the fluorescence signal for low Br concentrations becomes significantly small with respect to the tail of the Compton peak. It is generally considered that the signal should be at least 3 times the background, and then the Br concentration detection limit is about 23ppm (0.3 mM). This value is consistent with lowest concentrations previously mentioned for XAS measurement on BM30B/CRG-FAME at ESRF[1] and on BioCAT at APS[20].

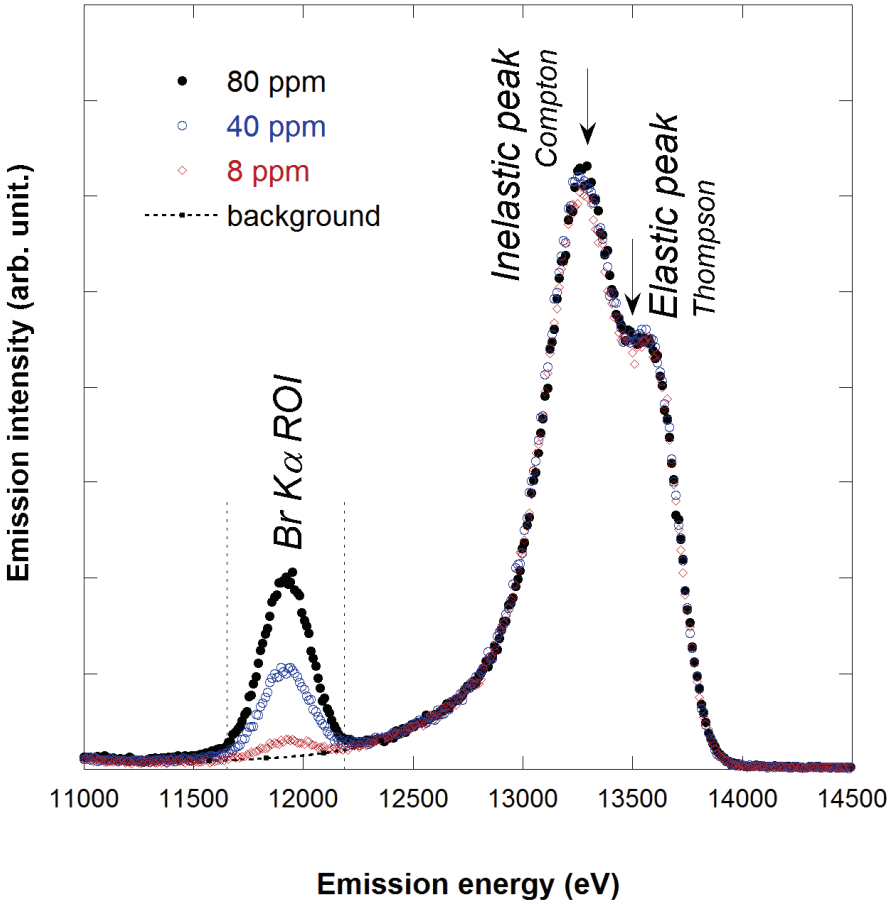

FIGURE 2. Influence of scattered beams on X-ray fluorescence emission spectra collected using the CANBERRA 30-elements SSD for bromide aqueous solutions at different concentrations.

C. Spatial resolution

Solid state detectors do not have any spatial detection resolution. Thus, any fluorescence, elastic and inelastic scattering signal from a sample holder, or more generally from the experimental setup, cannot be filtered. One solution is to install fluorescence soller slits between the sample and the detector but this does not give significant improvement[21].

IV. SPECTROMETER

A. Mechanics

The spectrometer has been entirely designed by the staff of the BM30B/CRG-FAME beamline and built at the Néel Institute (CNRS, Grenoble).

During the design, emphasis was given to user-friendly operation and on high adaptability of the sample environment. Different views of the spectrometer are shown in FIG

4: a top-view of the final drawing, a detailed view of the mechanical assembly of crystal and a 3D view with the 5 Rowland circles that intersect at the sample and detector points. The main parameters of the spectrometer and characteristics are summarized in Table 1.

TABLE 1. Technical parameters of the spectrometer

Bragg angle range (°)		45 - 86
Crystal bending radius (m)		0.5
Crystal diameter (m)		0.1
Total mass (kg)		100
y axis translation	Length (mm)	250
	Precision (μm)	10
Adjustment δz axis translation	length (mm)	10
	Precision (μm)	2
z_{det} axis translation	length (mm)	500
	Precision (μm)	10

As already mentioned[12], all the different mechanical motions are achieved using standard linear (y and z) and rotation (γ and $\delta\theta$) motorized stages. The role of the rotation stages is to align vertically the bent crystal*, i.e.* place the crystal in a normal position to the y axis. These adjustments - verticality and normality - of the crystals are achieved during the preliminary alignment procedure; these motions are not used during energy scans. Each crystal is therefore always in vertical position. For this reason, the mechanical angular ranges of the rotation stages are limited to ±2°. The technological solutions for the hinges are weak link systems as they allow a precise positioning, without any mechanical clearance. Following the same idea, the individual height of the 5 crystals can be finely adjusted (δz motion, FIG. 3) in order to compensate for small variations of the crystals characteristics, such as the radii of curvature. The Bragg energy selection is then achieved using only the linear motions along the perpendicular beam axis (y) and vertical axis (z). For this purpose, large high-load linear

motions are used for the long-range linear movements. The five y-translation motions are fixed on an aluminum alloy (Fortal) plate with a 27.5° offset angle between two adjacent translations. The detector is placed on 4 motorized motions (1 rotation and 3 translations) to position it at the desired angle, just above the sample and at the focal point.

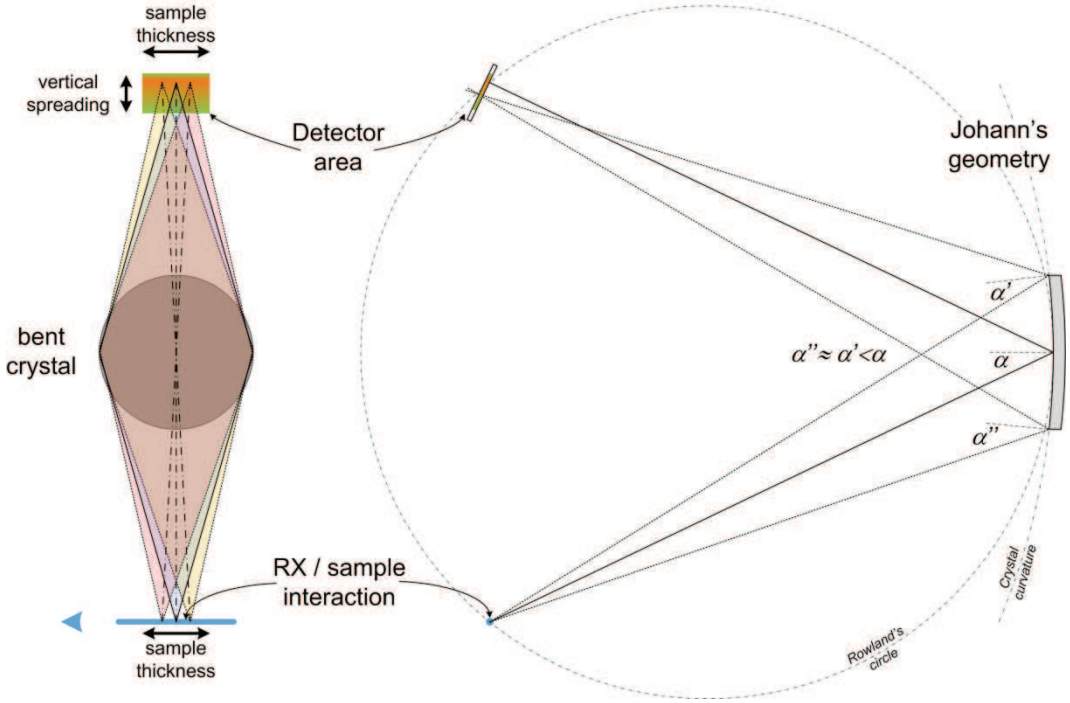

FIGURE 3. Visualisation of the intersection between the incident beam and the detection cone and resolution effect - vertical spreading of the focal spot on the detector.

With such mechanical and technical characteristics, the attainable Bragg angle ranges from 45 to 86°. The lower limit of 45° was arbitrary fixed during the conception phase. For such low Bragg angles, the energy resolution of the spectrometer is poor due to the Johann geometry error (see for example ref 27). The higher limit is a consequence of the Rowland circle geometry used: for a Bragg angle of 90°, the ideal detector position is on the sample. Thus, due to the spatial clearance necessary to install large sample environment set-ups, we set the higher limit to 86°.

Such a geometry (each crystal is maintained vertically, the detector is above the sample), allows to increase the number of crystals symmetrically around the axis sample-

detector. The different Rowland circles intersect then exactly at the same points, the sample and the detector, without any additional angular adjustment. This geometry is also used for example in a 5-crystal[22], 14-crystal[23,24] and 40-crystal[24] spectrometers installed on the 6-2 beamline at SSRL.

The spectrometer uses in total 21 small stepper motors to control all the motions: 4 stepper motors for each crystal bloc, one for the main vertical translation and 3 for the detector motions. Many commercial electronics for such devices exist but our choice was to develop our own controller, with less features and less versatile than commercial devices, but clearly cheaper. We chose to use WAGO modules, an 750-841 Ethernet 100 Mbit/s TCP/IP programmable fieldbus controller, and stepper motor modules for current up to 1.5 A. The commands necessary to control the motors are sent *via* ESRF standard control program SPEC[25] to each rack controller. The main advantages of our system are its small size, a connection via Ethernet, a standalone operation feature to test the motor either with a web client or console based program, and the low cost. The spectrometer can be relatively easily removed from the beamline, and reinstalled and controlled by a laptop anywhere.

B. Optics

Different geometries exist depending on the application: Cu foil absorber coupled to a point focusing spatial filter[26] for XRS, Bent crystal Laue analyzer in a logarithmic spiral shape[27,28,29,30] (Zhong, Kropf, Adams, Kalaja,) for XAFS. We choose to work with spherical bent crystals in the Johann geometry[31].

Spherically bent crystals (0.5 m bending radius) with a diameter of 0.1 m are used as dispersive optical elements in the spectrometer. The crystals are assembled as already described by Collart and co-workers[31]. High resolution X-ray analyzers are obtained using anodic bonding technique, which is a method of permanently joining glass to silicon without the use of adhesives. This method is a common process used in microelectronics device fabrication. The analyzer consists of a 225 μm thick silicon wafer spherically bent between convex and concave polished PYREX glass substrates of 0.5 m curvature radius. A dedicated experimental set-up has been developed by the 'Cellule Project' of the Institut de Minéralogie et Physique des Milieux Condensés in order to clamp silicon wafer and glass substrates at high force (1500 N) and high temperature (~ 350°C). A high DC potential (up to >1.7 kV) is then applied between silicon and glass creating an electrical field which drifts the ions in the glass. The depletion of sodium ions near the surface and the creation of surface charge

generate a large electrostatic force and bring the silicon and glass into intimate contact, eventually creating chemical bonds. Such analyzers have been successfully produced and have improved the energy resolution[31].

Currently, spherically bent Si crystals with (111) and (110) orientations are available on the beamline. They have been characterized by measuring the energy resolution on the spectrometer (see § III.D). Two others orientations (331) and (311) will be available in the future. These sets of different crystals will allow to cover a broad energy range from 4 to 19.7 keV. Such an energy range is sufficient to probe the Kα, Kβ, Lα and Lβ fluorescence lines of all the elements from Ca (Z = 20) to U (Z = 92).

C. Detection

In the Rowland circle geometry, the detector is located above the sample, along the z_{det} axis (FIG. 4). The total path length from the sample to the diffracting bent crystal and then to the detector equals 1 m; therefore operation under helium atmosphere is compulsory in order to minimize the absorption, especially in the low-energy region (from 4 to 8 keV).

Currently, two detectors are available. The first one is a 5 mm thick NaI(Tl) scintillator from FBM Oxford with a large active surface (7 cm^2), an energy resolution of 50% and a low maximum counting rate. The second detector is a silicon drift detector (SDD) from SII Nanotechnology (VORTEX-90EX®) with a small active area (50 mm^2) and a high dynamic range, it is also more compact and offers a useful energy resolution (2-4%).

The use of a 2D hybrid pixel detector such as XPAD3S[32] (soon available on the beamline), Pilatus[33], Medipix2[34] is also possible. The advantage of using 2D detectors is the possibility to have a single threshold adjustable per pixel and so to suppress the background counts (as with the SDD). Moreover such a detector can be used to isolate the appropriate signal induced by the X-ray beam - sample interaction, so as to discriminate the signals from the sample and from its container. Finally it also allows to focus the diffracted photons on different areas on this detector, to monitor each crystal separately.

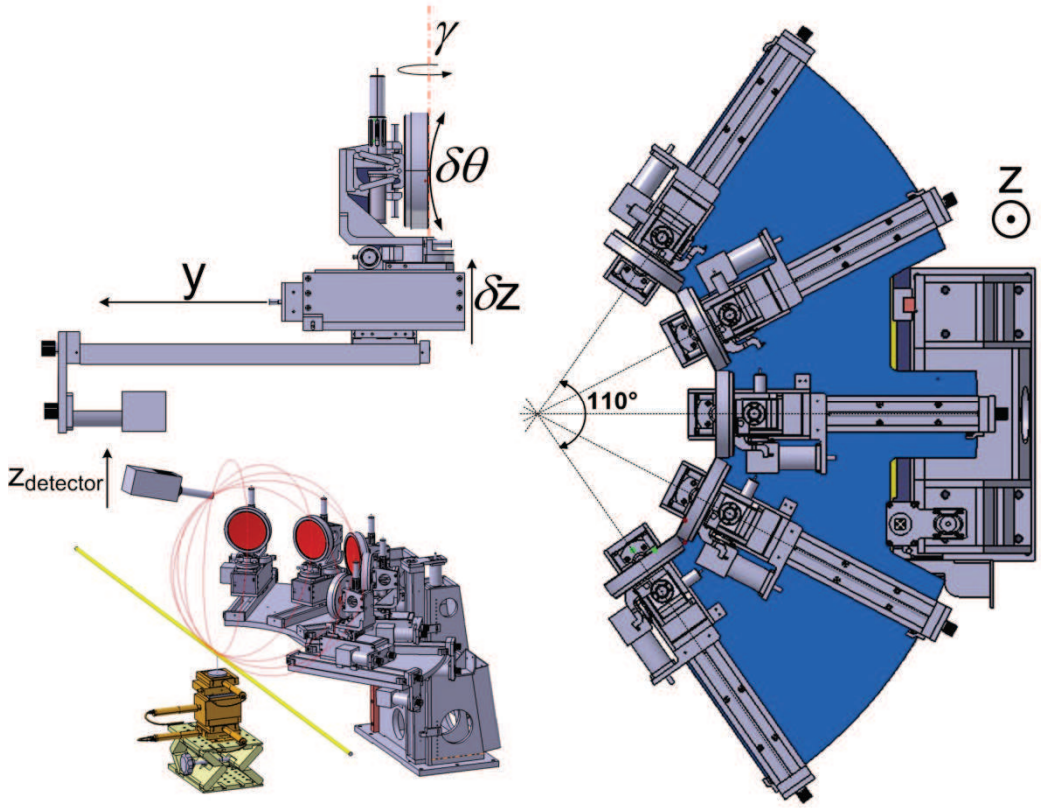

FIGURE 4. View of the spectrometer: detail of crystal assemblage (left – top position), view of the spectrometer on the beamline with the Vortex EX-90 as detector (left – down position) and top-view of a spectrometer drawing (right).

D. Theoretical and experimental resolutions

The global theoretical resolution of the spectrometer includes both the incident beam characteristics (the beam vertical size, h, -$\Delta E_{\text{beam vertical size}}$-) and those of the crystal (the intrinsic resolution of the chosen reflexion at the emission energy E -$\Delta E_{\text{reflexion}}$-, the Johann's approximation -ΔE_{Johann}-):

$$\Delta E_{beam\ vertical\ size} = 2 \times E \times \frac{\tan^{-1}[h \times \cos(\frac{\frac{\pi}{2}-\theta}{2000 \times R})]}{\tan\theta}$$

$$\Delta E_{reflexion} = E \times (2.26 \times 10^{-7}) \times f_{hkl} \times \begin{pmatrix} 8\ if\ hkl\ even\ and\ h+k+l=4n \\ 4\sqrt{2}\ if\ hkl\ odd \\ 0\ otherwise \end{pmatrix}$$

$$\Delta E_{Johann} = 1000 \times \frac{E}{6} \times \frac{(\frac{50}{R})^2}{\tan^2\theta}$$

Where θ is the Bragg angle (°), E the fluorescence emission energy (eV), f_{hkl} the structure factor of the reflexion, R the crystal curvature radius (m) and h the vertical beam size (mm).

The contributions being independent, the total energy resolution ΔE_{CAS} of the spectrometer is the convolution of all these individual contributions. By approximating all these contributions as Gaussian functions, ΔE_{CAS} (can be easily calculated using the following formula:

$$\left(\Delta E_{CAS}\right)^2 = \left(\Delta E_{reflexion}\right)^2 + \left(\Delta E_{Johann}\right)^2 + \left(\Delta E_{beam\,vertical\,size}\right)^2$$

The experimental resolution is determined by recording the quasi-elastic peak of the incident beam from the sample. The FWHM of the peak, fitted by a Gaussian function, gives the total (incident beam and spectrometer contribution) experimental resolution value. Theoretical and experimental resolutions obtained for the first experiments are gathered in table 2.

TABLE 2. Experimental and theoretical resolutions for HERDF-XAS experiments.

Emission line	Crystal	Bragg angle (°)	Theoretical resolution (eV)	Best experimental resolution (eV)
Fe $K\alpha_1$ (6.404 keV)	Si(333)	67.9	1.9	2.3
Co $K\alpha_1$ (6.930 keV)	Si(440)	68.7	1.9	3.0
Fe $K\beta_1$ (7.058 keV)	Si(440)	66.1	1.9	2.0
Cu $K\alpha_1$ (8.048 keV)	Si(444)	79.3	0.7	1.4
Sr $K\alpha_1$ (14.165 keV)	Si(880)	65.7	5.0	12.9

As it can be seen, experimental values are in general worse than the theoretical expected values. However, for low *hkl* values, experimental resolutions are close to theoretical values while for high *hkl* value, a better resolution can be expected. This probably due to the microstrains developed during the crystal bending stage. Bending causes elastic deformations in the crystal structure which ultimately broaden the bandwidth of the reflection[35,36]. A solution to overcome this effect is to use diced analyzer crystals, which are built by fixing a large number, typically 10^4, of small flat single crystals (dices) on a spherical substrate, thus

providing a polygonal approximation to the Rowland circle geometry[37]. These crystals allow a better resolution: 10-300 meV for diced Si(nnn) crystals with n=3 to 7 to be compared with 500 – 2000 meV for bent Si(nnn)/Si(nn0) crystals with n = 3 to 8 for the same curvature radius[38].

The main effect of the Johann geometrical aberrations is on the energy resolution result. This is a consequence of a vertical spreading of the diffracted spot on the detector due to the incidence angle α of the X-ray arriving at the center of the bend crystal, higher than an X-ray arriving in another area of it (FIG. 3). To decrease this contribution and so to increase the energy resolution, it is possible to limit the detection area, *i.e.* to limit the crystal collecting area to its center.

V. EXPERIMENTAL VALIDATION

We have seen in § III several limitations of solid state detectors (saturation, energy and spatial resolution). This paragraph presents a solution to overcome some of these limitations. The first measurements were dedicated to XAFS spectroscopy applications: (i) the matrix fluorescence removal (see § III.A) with the study of Co adsorbed on iron oxide nanoparticles and (ii) the probe of a weak fluorescence at high energy (see § III.B) in a crystalline matrix with the example of diluted Sr in UO_2 simulated irradiated nuclear fuel.

A. Beyond the saturation: Co adsorbed on iron oxide nanoparticles

During the last decade, interest in nanotechnology and manufactured nanoparticles has grown and a wide range of applications for emerging nanomaterials has been proposed. For instance differences in reactivity might be exploited to improve surface-based reactions as it could be used for arsenic removal processes. Oxyhydroxide iron particles smaller than 20 nm exhibit an increase of adsorption capacity and those of 11 nm in diameter adsorbs 3 times more As per nm^2 than 20 nm particles[39,40,41].

In our experiment, we focus on the mechanisms of Co adsorption at the surface of nanomaghemite (γ-Fe_2O_3). The difficulty, here, is to probe an element (Co, atomic no. Z) adsorbed on another (Fe, atomic no. Z-1) which dominates the fluorescence signal. Co K-edge total fluorescence and High Energy Resolution Fluorescence Detected (HERFD)-XANES spectra are presented in FIG. 5.

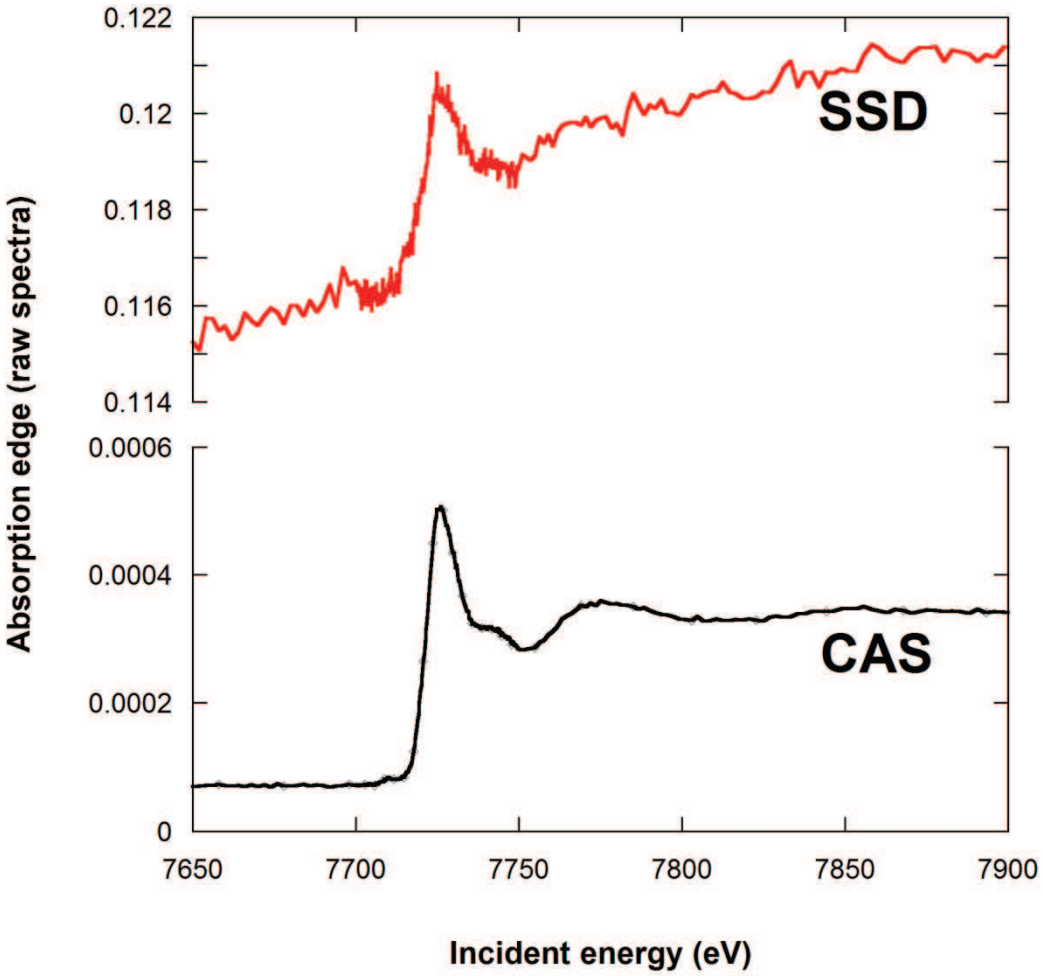

FIGURE 5. Co K-edge XANES of Co adsorbed on ferrihydrite collected in total fluorescence yield using a solid state detector (SSD) and in high energy resolution fluorescence detected using the crystal analyzer spectrometer (CAS). Integrated counts after edge are ~5.10^5 using SSD and ~4.10^4 using CAS for counting times of 6s and 120s respectively.

The integrated counts after edge are $4.8x10^5$ using SSD and $3.6x10^4$ using CAS corresponding to count-rates of 8.10^4 s^{-1} and 300 s^{-1} respectively. These values do not reflect the data quality. One way to quantify the detector efficiency for a given kind of sample is then to calculate the effective number of counts (N_{eff})[12] defined as $\frac{N_{signal}^2}{N_{signal}+N_{background}}$. For this particular system, N_{eff} is ~150 c/s for SSD and 250 c/s for CAS. In the last case, the total count-rate is dominated by useful events (250 out of 300 s^{-1}) are effective counts. It is thus reasonable to multiply the number of acquisitions to increase the data quality. Moreover, the background on CAS spectrum is very low, constant and due to photons scattered (not

diffracted) by the crystals. Inversely, the background on SSD spectrum is high and increases with energy. Independently from statistical considerations, the spectrum shape associated with very small absorption edge (~0.002) makes the normalization of SSD data very complicated for this particular system.

HERFD data have been analyzed and preliminary results show that with this high surface coverage, Co atoms are adsorbed on ferrihydrite surface.

B. Energy resolution: Sr in simulated irradiated UO_2 nuclear fuel.

One of the main goals of research in nuclear energy is to improve the economic and safety performance of nuclear fuels. One solution is to extend its life time in reactor. But in this case, the behavior of fission products becomes the limiting factor and more specifically their segregation/precipitation. Thus, increasing fuel burn up must be accompanied by an effort to improve our understanding of the nature and behavior of the material as fission products accumulate. One course of action is to collect experimental data relative to irradiated fuel. Due to the very high radioactivity of the samples, this data can only be obtained through post-irradiation examination of irradiated fuels in dedicated facilities. To overcome the former difficulty, the use of simulated high burn up UO_2 nuclear fuel, termed SIMFUEL, is a good alternative[42].

This experiment has a double interest. The first one is to probe a diluted element (Sr at 1400 ppm) in a crystalline UO_2 sample doped with 11 elements (Ba, Ce, La, Mo, Sr, Y, Zr, Rh, Pd, Ru, Nd) simulating the chemical composition of irradiated nuclear fuel. The second more technical interest is to see if we can limit the impact on the XAS spectra of the Bragg peaks originating from the well crystallized UO_2 matrix. For the experiment detailed here, we focused our interest on Sr.

The data are collected both in HERFD and total fluorescence modes at Sr K-edge. In total fluorescence detection using SSD, the XANES/EXAFS spectra cannot be exploited due to Bragg peaks in the pre-edge and at the end of the EXAFS region (FIG. 6). Several orientations of the sample relative to the incident beam are tested but provided no improvement. However, different solutions exist to reduce the spurious signal given by Bragg peaks using rotating[43] or vibrating[44] sample holder. With such systems, the Bragg peak energy position changes with the sample angular orientation. By integrating the absorption signal on different angular positions, Bragg peaks are averaged on a given energy range. They are not deleted but their effects are effectively reduced.

Using the CAS, this unwanted diffraction signal does not interfere with the absorption. Indeed, the photons diffracted (so elastically scattered) by sample crystallites are not detected by the CAS since their energy is different from the selected fluorescence line energy (in this case Sr $K\alpha_1$). This enables us to probe a relatively diluted element (Sr) within the UO_2 crystalline matrix.

Based on the comparison and a linear combination fitting, the HERFD spectra analysis demonstrates that Sr is distributed between two chemical forms: SrO type (40%) and a perovskite $SrZrO_3$ type (60%).

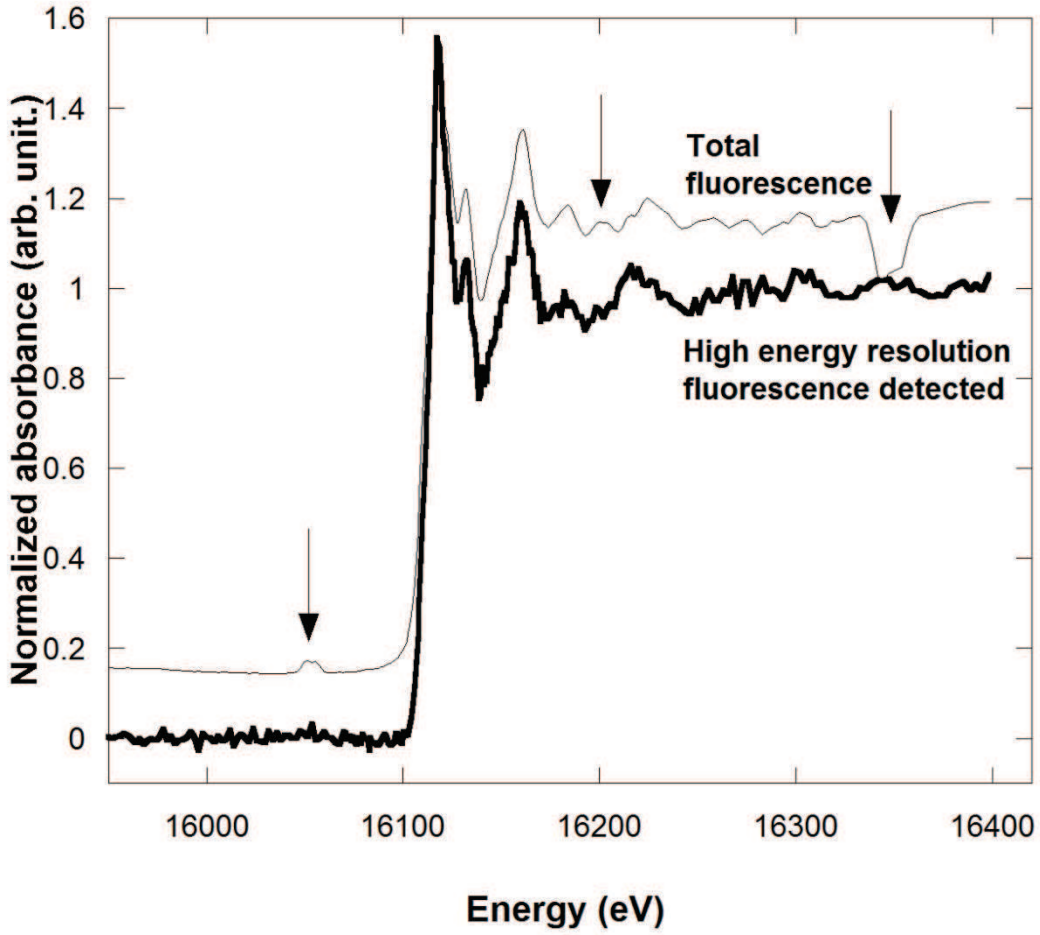

FIGURE 6. Normalized Sr K-edge XANES spectra collected in total fluorescence (SSD) and HERDF mode (CAS) on a crystalline UO_2 sample doped with 1400 ppm Sr. The arrows signal parasite effects due to Bragg peaks from UO_2 matrix.

VI. DISCUSSION: SSD *vs.* CAS

As already mentioned, the main application of this spectrometer on BM30B/CRG-FAME beamline is the matrix fluorescence removal. In this case, it is interesting to compare total fluorescence and HERFD modes, and thus quantify in which case using a CAS is more appropriate than a SSD. We chose here to develop this idea in the particular case of Co included in a Fe-rich matrix[45]. In this particular experiment (§ V.A), the interest of using the CAS is shown in FIG. 7 which represents typical emission fluorescence spectra collected with the CAS and the SSD. Each elementary fraction of the crystal can be considered as a perfect crystal. To the first order, this part is diffracting / reflecting all the photons of energy E_{CAS} within its angular / energetic acceptance: $\delta\Delta E_{CAS} = \omega_{Darwin} \times E_{CAS}$.

The value equals around 0.069 eV for the *Kα1* fluorescence energy of Co and the Si(440) crystals. We assume that there is no other contribution than the selected fluorescence photons: no contribution from the scattered photons (from the sample or from the crystals) and from the fluorescence lines tails of the main constituents of the sample. The signal received by the detector of the CAS system centered around the *Kα1* fluorescence energy of Co (energy width of the emission line: $\Delta E_{K\alpha 1}$) after optimization of the spectrometer ($E_{K\alpha 1} = E_{CAS}$) can be then expressed as:

$$S_{CAS} = (I_{K\alpha 1})_{Co} \times \sigma_{CAS} \times \frac{\delta\Delta E_{CAS}}{\Delta E_{K\alpha 1}}$$

Where σ_{CAS} is the spectrometer cross-section.

Conversely, the signal measured with a SSD with a typical energy resolution around 250 eV includes the contribution of 1) the entire $K\alpha_1$ and $K\alpha_2$ fluorescence lines of Co and 2) the Kβ fluorescence lines of Fe as a background:

$$S_{SSD} = \left[(I_{K\alpha 1} + I_{K\alpha 2})_{Co} + \left(I_{K\beta}\right)_{Fe}\right] \times \sigma_{SSD}$$

$$(I_{K\alpha 1})_{Co} = \omega_{Co} \times [Co] \times \rho_{sample} \times \mu_{Co}(E_{incident}) \times I_0(E_{incident})$$

$$(I_{K\alpha 2})_{Co} = 0.5 \times (I_{K\alpha 1})_{Co} \times I_0(E_{incident})$$

$$\left(I_{K\beta}\right)_{Fe} = 0.17 \times (I_{K\alpha 1})_{Fe} = 0.17 \times \omega_{Fe} \times [Fe] \times \rho_{sample} \times \mu_{Fe}(E_{incident}) \times I_0(E_{incident})$$

Where σ_{SSD} is the SSD cross-section and $\omega_{Co,Fe}$, $\mu_{Co,Fe}$, ρ_{sample} are the Co and Fe fluorescence yield, absorption probabilities, the sample volume mass and, incident flux.

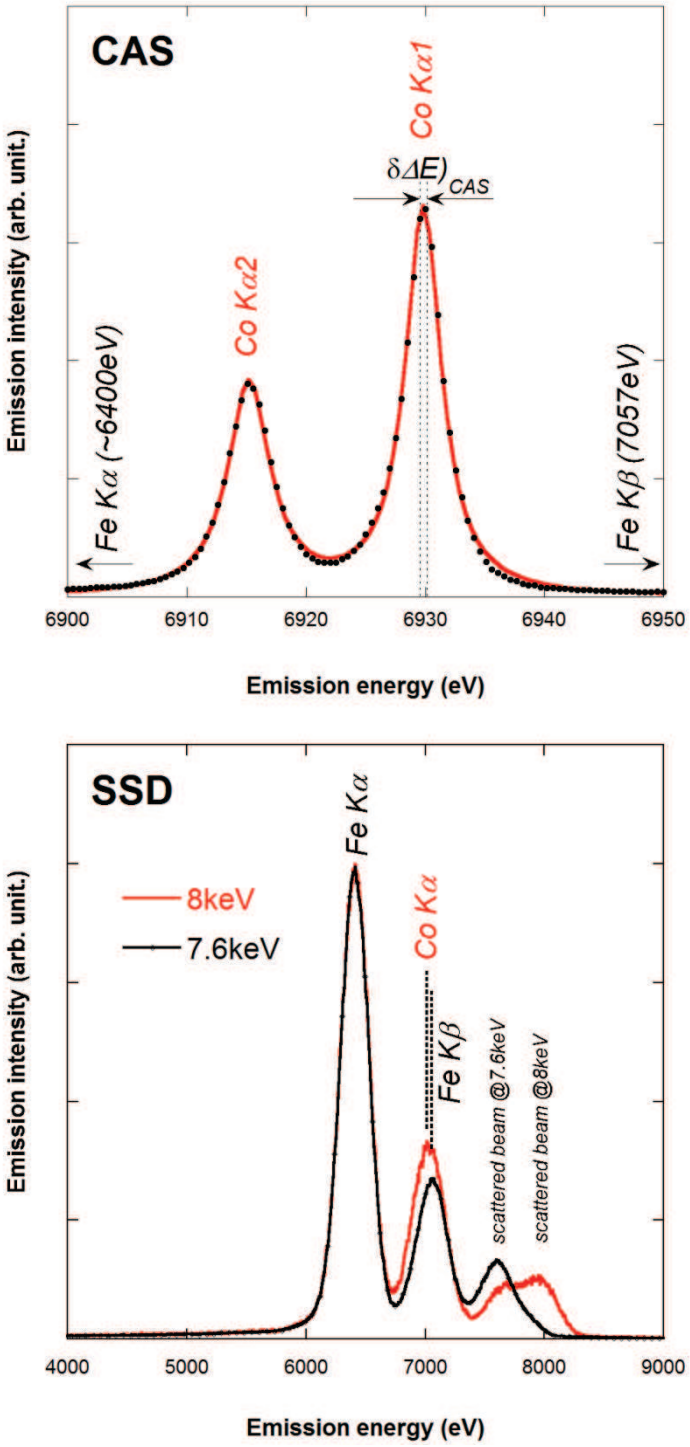

FIGURE 7. Fluorescence spectra measured using the high resolution crystal analyzer spectrometer (top) and the 30-element solid state detector (bottom) on Co adsorbed on nano-γFe_2O_3.

We used the formalism developed by Bunker[46] to estimate the number of effective counts. For the CAS, we reasonably assume that the signal is only due to the Co fluorescence contribution:

$$\left(N_{eff}\right)_{CAS} = (I_{K\alpha1})_{Co} \times \sigma_{CAS} \times \frac{\delta\Delta E_{CAS}}{\Delta E_{K\alpha1}}$$

On the other hand, for the SSD the contribution of the background has to be considered:

$$\left(N_{eff}\right)_{SSD} = \frac{(I_{K\alpha1} + I_{K\alpha2})_{Co}}{1 + \frac{\left(I_{K\beta}\right)_{Fe}}{(I_{K\alpha1} + I_{K\alpha2})_{Co}}} \times \sigma_{SSD}$$

$$\left(N_{eff}\right)_{SSD} = \frac{(I_{K\alpha1} + I_{K\alpha2})_{Co}}{1 + \frac{0.17 \times \omega_{Fe} \times [Fe] \times \mu_{Fe}(E_{incident})}{1.5 \times \omega_{Co} \times [Co] \times \mu_{Co}(E_{incident})}} \times \sigma_{SSD}$$

Another possibility to express when there is an advantage to use the CAS *vs.* the SSD is to estimate when the noise is smaller with one system or with the other:

$$noise_{SSD} = \frac{1}{\sqrt{(N_{eff})_{SSD}}} \text{ and } noise_{CAS} = \frac{1}{\sqrt{(N_{eff})_{CAS}}}$$

$$\frac{noise_{CAS}}{noise_{SSD}} = \sqrt{\frac{1.5}{1 + \frac{0.17 \times \omega_{Fe} \times [Fe] \times \mu_{Fe}(E_{incident})}{1.5 \times \omega_{Co} \times [Co] \times \mu_{Co}(E_{incident})}} \times \frac{\Delta E_{K\alpha1}}{\delta\Delta E_{CAS}} \times \frac{\sigma_{SSD}}{\sigma_{CAS}}}$$

Calculations are performed with σ_{CAS} and σ_{SSD} equal 0.3 and 0.0013, respectively and considering that the conditions are identical, *i.e.* sample, $I_0(E_{incident})$, the SSD at 25 cm from the sample with the element size of 5x5mm² (solid angle: 4.10^{-4} sr), all paths under vacuum, the number of emitted photons and the integration time are the same (FIG. 8).

FIG. 8 shows that it is often preferable to use a CAS instead of a 13-element SSD. Detection systems available on BM30B/FAME beamline, *i.e.* CAS and 30-element SSD, are also compared with μ_{Fe} ($E_{incident}$) = 305.6 $cm^2.g^{-1}$ and μ_{Co} ($E_{incident}$) = 324.8 $cm^2.g^{-1}$ at 8 keV, ω_{Fe} = 0.340 and ω_{Co} = 0.373[47], leads to a $\left(\frac{[Co]}{[Fe]}\right)_{limit}$ equal to 0.015 if using 5 crystals.

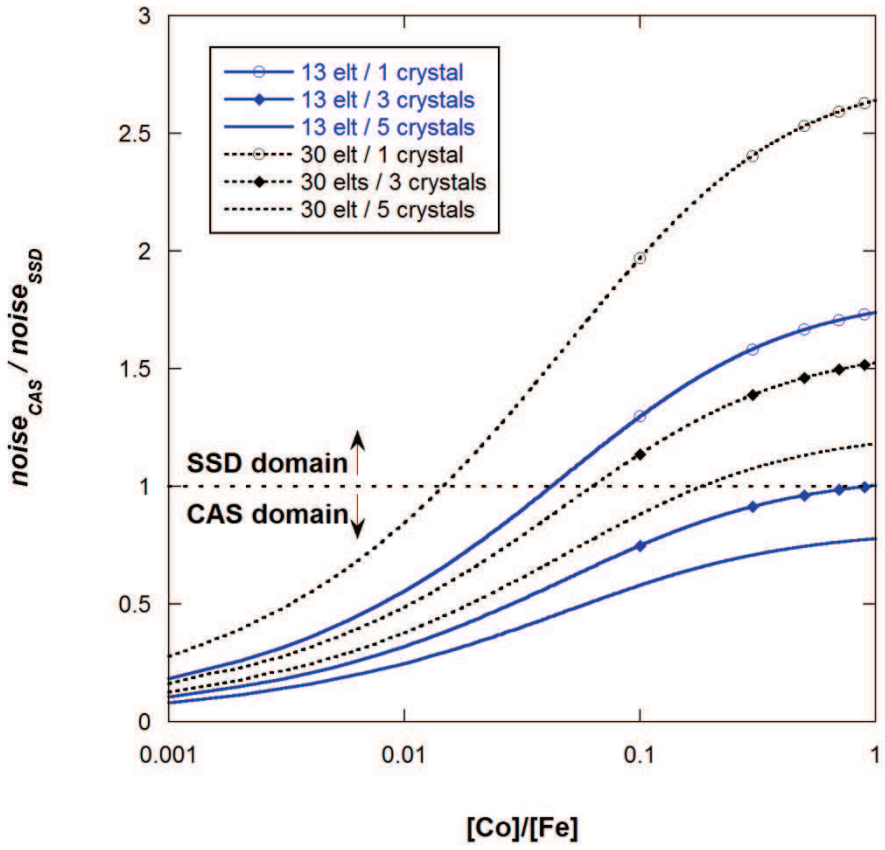

FIGURE 8. Comparison of the CAS with 13-element and 30-element SSD to determine which is the more appropriate in the case of Co adsorbed on iron sample.

VII CONCLUSIONS

A high resolution spectrometer in Johann geometry has been built and commissioned on BM30B/FAME beamline at the ESRF. It is now available for user operation. The feasibility of challenging experiments is demonstrated by test cases like HERFD XAS in samples that are difficult to measure with energy-dispersive detectors, *e.g.* Co adsorbed on iron oxide samples and Sr included within crystalline UO_2.

The spectrometer have been also duplicated and successfully tested on the MARS beamline dedicated to the characterization of radioactive samples at SOLEIL synchrotron[48].

ACKNOWLEDGEMENTS

This project is financially supported by the ANR NANOSURF (coordinator: C. Chaneac, Laboratoire de Chimie de la Matière Condensée de Paris, France), CEREGE laboratory (Aix en Provence, France) and the INSU CNRS institute.

[1] O. Proux, X. Biquard, E. Lahera, J.-J. Menthonnex, A. Prat, O. Ulrich, Y. Soldo, P. Trévisson, G. Kapoujyan, G. Perroux, P. Taunier, D. Grand, P. Jeantet, M. Deleglise, J-P. Roux and J-L. Hazemann, Physica Scripta **115**, 970 (2005).

[2] G. D. Pirngruber, J-D Grunwaldt, J. A. van Bokhoven, A. Kalytta, A. Reller, O. V. Safonova and P. Glatzel, J. phys. Chem. B **110**, 18105 (2006).

[3] V. A. Safonov, L. N. Vykhodtseva, Y. M. Polukarov, O. V. Safonova, G. Smolentsev, M. Sikora, S. G. Eeckhout and P. Glatzel, J. phys. Chem. B **110**, 23192 (2006).

[4] P. Glatzel, L. Jacquamet, U. Bergmann, F. M. F. de Groot and S. P. Cramer, Inorg. Chem. **41**, 3121 (2002).

[5] U. Bergmann, P. Glatzel and S. P. Cramer, Microchem. Journal **71**, 221 (2002).

[6] M. Krisch and F. Sette, Surf. Rev. Lett. **9**, 969 (2002).

[7] H. Hayashi, Y. Udagawa, W. A.Caliebe, and C. Kao, Chem. Phys. Lett. **371**, 125 (2003).

[8] F. de Groot, Chem. Rev. **101**, 1779 (2001).

[9] A. Kotani and S. Shin, Rev. Mod. Phys. **73**, 203 (2001).

[10] W. Schülke, Series of Synchrotron Radiation 7, edited by J. Chikawa, J. R. Helliwell and S. W. Lovesey. Oxford: Oxford Science (2007).

[11] J.-P. Rueff and A. Shukla, Rev. Mod. Phys. **82**, 847 (2010).

[12] J.-L. Hazemann, O. Proux, V. Nassif, H. Palancher, E. Lahera, C. Da Silva, A. Braillard, D. Testemale, M.-A. Diot, I. Alliot, W. Del Net, A. Manceau, F. Gélébart, M. Morand, Q. Dermigny and A. Shukla, J. Synchrotron Rad. **16**, 283 (2009).

[13] F. Rodolakis, P. Hansmann, J.-P. Rueff, A. Toschi, M.W. Haverkort, G. Sangiovanni, T. Saha-Dasgupta, K. Held, M. Sikora, I. Alliot, J.-P. Itié, F. Baudelet, P. Wzietek, P. Metcalf, and M. Marsi, Phys; Rev; Lett; **104**, 047401 (2010).

[14] O. Proux, V. Nassif, A. Prat, O. Ulrich, E. Lahera, X. Biquard, J-J Menthonnex and J.-L. Hazemann, J. Synchrotron Rad. **13**, 59 (2006).

[15] J.-L. Hazemann, K. Nayouf and F. de Bergevin, Nucl. Intr. Meth. B **97**, 547 (1995).

[16] J. C. Woicik B. Ravel, D. A. Fischer and W. J. Newburgh, J. Synchrotron Rad. **17**, 409 (2010).

[17] U. Fano. Phys. Rev. **72,** (1947).

[18] M. Frank, S. Friedrich, J. Höhne and J. Jochum, J. X-Ray Science and Technology **11**, 83 (2003).

[19] D. Testemale, R. Argoud, O. Geaymond and J.-L. Hazemann, Rev. Sci. Instrum. **76**, 043905 (2005).

[20] R. Fischetti, S. Stepanov, G. Rosenbaum, R. Barrea, E. Black, D. Gore, R. Heurich, E. Kondrashkina, A.J. Kropf, S. Wang, K. Zhang, T.C. Irving, and G.B. Bunker, J. Synchrotron Rad. **11**, 399-405 (2004).

[21] E.A. Stern and Heald, Rev. Sci. Instrum. **50**, 1579 (1979).

[22] P. Glatzel and U. Bergmann, Coord. Chem. Rev. **249,** 65 (2005).

[23] Y. Pushkar, X. Long, P. Glatzel, G. W. Brudvig, G. C. Dismukes, T. J. Collins, V. K. Yachandra, J. Yano and U. Bergmann, X-ray Spectroscopy **49**, 800 (2010).

[24] D. Sokaras, D. Nordlund, T.-C. Weng, R. Alonso Mori, P. Velikov, D. Wenger, A. Garachtchenko, M. George, V. Borzenets, B. Johnson, Q. Qian, T. Rabedeau and U. Bergmann, Rev. Sci. Instrum. **83**, 043112 (2012).

[25] http://www/certif.com/spec.html

[26] G.T. Seidler and Y. Fenga, Nucl. Instrum. Meth. Phys. Res. A **469**, 127(2001).

[27] Z. Zhong, D Chapman, B Bunker, G. Bunker, R. Fischetti and C. Segre, J. Synchrotron Rad. **6**, 212 (1999).

[28] A. J. Kropf, R. J. Finch, J. A. Fortner, S. Aase, C. Karanfil, C. U. Segre, J. Terry, G. Bunker and L. D. Chapman, Rev. Sci. Instrum. **74**, 4696 (2003).

[29] B. W. Adams and K. Attenkofer, Rev. Sci. Instrum. **79**, 023102 (2008).

[30] N. G. Kujala, C. Karanfil and R. A. Barrea, Rev. Sci. Instrum. **82**, 063106 (2011).

[31] E. Collart, A. Shukla, F. Gélébart, M. Morand, C. Malgrange, N. Bardou, A. Madourib and J-L Pelouard, J. Synchrotron Rad. **12**, 473 (2005).

[32] K. Medjoubi, T. Bucaille, S. Hustache, J-F. Bérar, N. Boudet, J-C. Clemens, P. Delpierre and B. Dinkespiler, J. Synchrotron Rad. **17**, 486 (2010).

[33] P. Kraft, A. Bergamaschi, C. Broennimann, R. Dinapoli, E. F. Eikenberry, B. Henrich, I. Johnson, A. Mozzanica, C. M. Schlepütz, P. R.Willmott, and B. Schmitt, J. Synchrotron Radiat. **16**, 368 (2009).

[34] X. Llopart, M. Campbell, R. Dinapoli, D. San Segundo, and E. Pernigotti, IEEE Trans. Nucl. Sci. **49**, 2279 (2002).

[35] S. Takagi, Acta Cryst **15**, 1311 (1962).

[36] S. Takagi, J. Phys. Soc. Jap. **26**, 1239 (1969).

[37] S. Huotari, F. Albergamo, Gy. Vankó, R. Verbeni, and G. Monaco, Rev. Sci. Instrum. **77**, 053102 (2006).

[38] R. Verbeni, T. Pylkkänen, S. Huotari, L. Simonelli, G. Vanko, K. Martel, C. Henriquet and G. Monaco, J. Synchrotron Rad. **16**, 469 (2009).

[39] S. Yean, L. Cong, C. T. Yavuz, J. T. Mayo, W. W. Yu, A. T. Kan, V. L. Colvin, and M. B. Tomson, J. Mater. Res., **20**, 3255-3264 (2005).

[40] M. Auffan, J. Rose, O. Proux, D. Borschneck, A. Masion, P. Chaurand, J.-L. Hazemann, C. Chaneac, J-P. Jolivet, M. R. Wiesner, A. Van Geen, and J-Y. Bottero. Langmuir **24**, 3215-3222 (2008).

[41] G. Morin, G. Ona-Nguema, Y.H. Wang, N. Menguy, F. Juillot, O. Proux, F. Guyot, G. Calas, and G.E. Brown Jr, Environ. Sci; Technol. **42**, 2361–2366 (2008).

[42] P.G. Lucuta, R.A. Verrall, Hj. Matzke, B.J. Palmer, J. Nucl. Mater. **178**, 48-60 (1991).

[43] S. Pasternak, F. Perrin, G. Ciatto, H. Palancher, and R. Steinmann, Rev. Sci. Instrum. **78**, 075110 (2007).

[44] M. Tormen, D. De Salvador, M. Natali, A. Drigo, F. Romanato, F. Boscherini, and S. Mobilio, J. Appl. Phys. **86**, 2533 (1999).

[45] See supplementary material at [**URL will be inserted by AIP**] for the complete calculations in the general case of an element probe within a fluorescent matrix

[46] G. Bunker, Cambridge University Press, Cambridge UK (2010).

[47] M.O. Krause and J.H. Oliver, J. Phys. Chem. Ref. Data **8**, 308 (1979).

[48] B. Sitaud, P. L. Solari, S. Schlutig, I. Llorens, and H. Hermange, J. Nucl. Mater. **425**, 238 (2012).